

Development and Testing of Conventional and Additively Manufactured Aerospike Nozzles for Small Satellite Hybrid Propulsion

Stephen A. Whitmore^{*} and Isaac W. Armstrong[†]
Utah State University, Logan Utah, 84322-4130

The Aerospike Nozzle is well-known for altitude compensating capability; however, the aerospike also presents the advantage of a small form factor at high expansion ratios. Aerospike nozzles can be more than 75% smaller than a conventional nozzle with the same expansion ratio. This feature presents a significant potential for volumetric improvements of SmallSat scale space propulsion systems. This research campaign quantitatively assesses the potential advantages of using an aerospike nozzle for a small-scale hybrid propulsion system. Two aerospike nozzles were fabricated during the course of this development campaign, one using conventional manufacturing methods, and one leveraging the capabilities of modern 3-D printing. The conventionally manufactured nozzle was fabricated from graphite, stainless steel, and aluminum, and consisted of a complex assembly with multiple pieces. The second nozzle was manufactured using 3-D laser sintering technology, and was printed as a single piece from Inconel 718 super-alloy. The aerospike contours were integrated into an existing small-scale hybrid motor that had been previously tested using both optimally-expanded and over-expanded conventional fixed-geometry nozzles. Both ambient and vacuum tests were performed, with the conventional and 3-D fabricated aerospike nozzles exhibiting equivalent performance and burn lifetimes. Both aerospike nozzles exhibited superior performance compared to conventional fixed-geometry nozzles.

Nomenclature

Symbols

A_c	= fuel port cross-sectional area, cm^2
A_e	= nozzle exit area, cm^2
A_s	= cross sectional area at shock wave position, cm^2
A_1	= venturi inlet area, cm^2
A_2	= venturi outlet area, cm^2
A^*	= cross sectional area at which local flow chokes, cm^2
C_F	= thrust coefficient
c_e	= effective exhaust velocity, m/s
G_{ox}	= oxidizer massflux, g/cm^2-s
G_{tot}	= total massflux, g/cm^2-s
I_{sp}	= specific impulse, sec
L	= fuelgrain length, cm

^{*} Professor, Mechanical and Aerospace Engineering Department, 4130 Old Main Hill, AIAA Associate Fellow

[†] Graduate Research Assistant, Mechanical and Aerospace Engineering Department, AIAA Student Member

M_1	=	Mach number upstream of shock wave
M_e	=	exit plane mach number with embedded shock wave
ΔM_{fuel}	=	consumed fuel mass, <i>g</i>
\dot{m}_{fuel}	=	fuel massflow, <i>g/s</i>
\dot{m}_{ox}	=	oxidizer massflow, <i>g/s</i>
\dot{m}_{total}	=	total massflow through the nozzle, <i>g/s</i>
O/F	=	oxidizer/fuel ratio
P_1	=	venturi inlet pressure, <i>psia</i>
P_2	=	venturi throat pressure, <i>psia</i>
P_0	=	venturi flow path stagnation pressure, <i>psia</i>
P_{02}/P_{01}	=	stagnation pressure ratio across shock wave
R_g	=	gas constant, <i>J/kg-K</i>
r_L	=	longitudinal average of the fuel port radius, <i>cm</i>
r_0	=	initial fuel port radius, <i>cm</i>
T	=	venturi flow path temperature, <i>K</i>
T_0	=	stagnation temperature, <i>K</i>
t	=	burn time, <i>s</i>
η^*	=	combustion efficiency
ε	=	nozzle expansion ratio, A_e/A^*
Φ	=	equivalence ratio
γ	=	ratio of specific heats
ρ_{fuel}	=	solid fuel density, <i>g/cm³</i>
$(\dot{\quad})$	=	time derivative, <i>()/s</i>

I. Introduction

Conventional fixed-geometry rocket nozzles allow optimum performance only at one specific ambient pressure or operating altitude. Thus, conventional nozzles necessarily represent a design compromise. In a conventional nozzle combustion gases are choked by a cylindrical throat and then expand through a diverging nozzle pathway, exchanging thermal energy for kinetic energy, and creating a large increase in momentum of the exit plume. The optimal operating condition for a conventional nozzle occurs when the pressure at the exit plane exactly equals the background ambient pressure, and this condition is rocket's set by the chamber pressure and expansion ratio. Figure 1 shows the flow fields associated with an over-expanded, optimally-expanded, and under-expanded bell nozzle.¹ For the conventional nozzle careful design is needed to achieve desired high altitude (under-expanded operating conditions) performance while avoiding flow separation and an embedded shock wave when operating at low altitudes (over-expanded operating conditions).

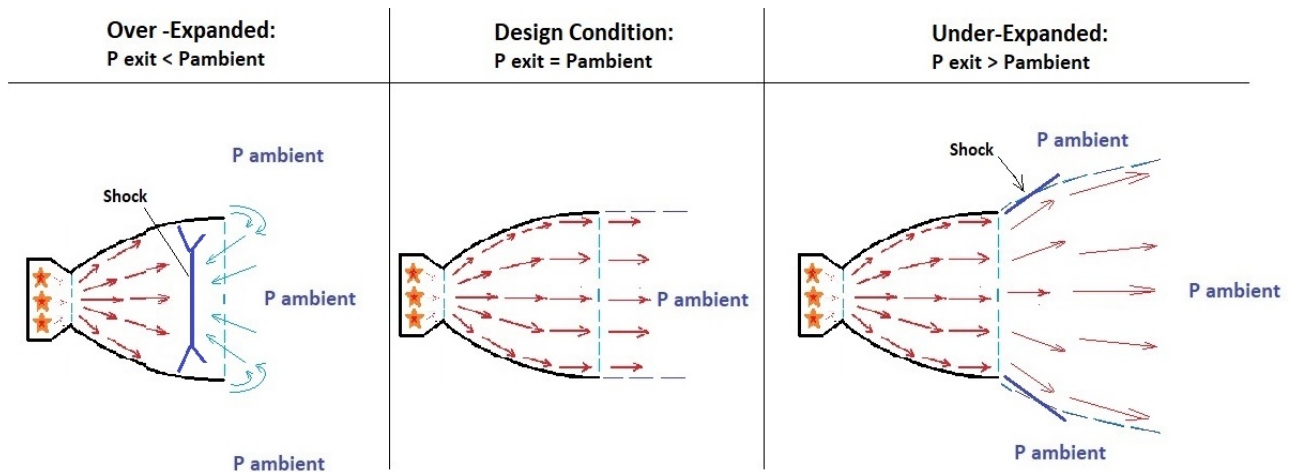


Figure 1. Over-Expanded, Optimally-Expanded, and Under Expanded Flow Regimes for a Conventional Fixed-Geometry Bell Nozzle.

The over-expanded nozzle develops an exit pressure that is less than the surrounding atmospheric pressure, and a locally negative pressure gradient results. When the negative pressure gradient becomes sufficiently strong, boundary layer separation and backflow can form along the nozzle walls. Backflow and flow separation typically result in the formation of an embedded shockwave. The embedded shock wave leads to a loss of performance, and possible structural failure due to high heating levels at the shock-wall interface and dynamic loads due to flow separation.

For under-expanded conditions the nozzle is fully started and isentropic; however, the exit plane pressure is substantially higher than ambient; meaning that the only a portion of the thermal energy of the plume has been recovered and converted into kinetic energy. The result is the potential for a considerable loss in the available nozzle momentum thrust. Consequently, typically lower expansion ratio nozzles are used for low altitude operation, and high expansion ratio nozzles are reserved for near-space operations. Few designs are able to bridge the gaps between operating altitudes.

Figure 2 shows the flow fields associated with the aerospike nozzle.^{2,3} For the aerospike nozzle, the external streamline is unconstrained, and the flow path is essentially opposite of a conventional nozzle. The plume flow is radially directed inward from an annular throat, with the plume being directly exposed to external flow streamline. The aerospike plume is thus directly coupled to the external environment, and is free to expand or contract based on the ambient pressure level. This feature allows for continuous altitude compensation. Consequently, a very high expansion ratio nozzle -- designed for efficient vacuum performance -- can also operate effectively and safely at low altitudes and higher operating pressures.

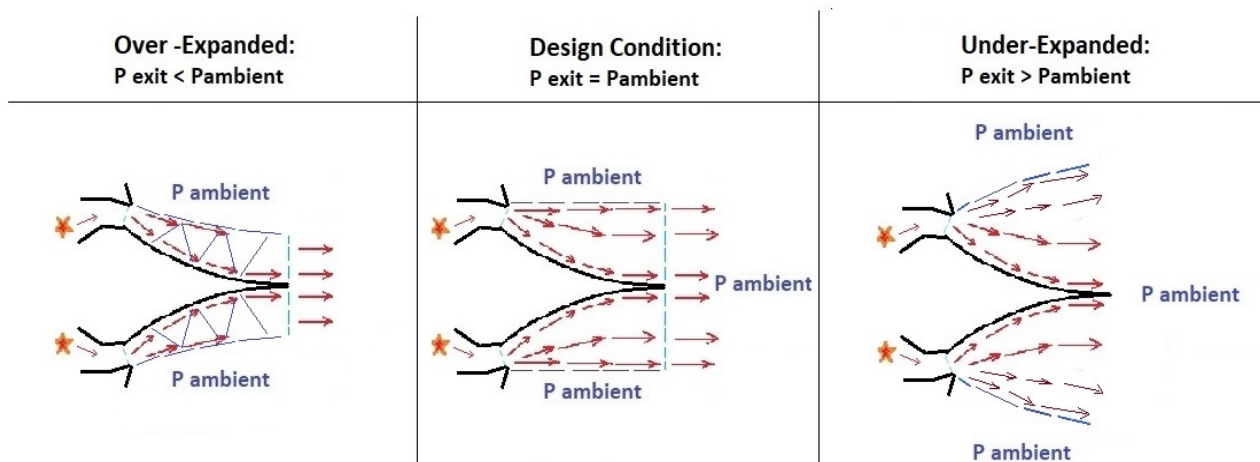


Figure 2. Over-Expanded, Optimally-Expanded, and Under Expanded Flow Regimes for an Aerospike Nozzle.

The aerospike nozzle shape has long been known for its potential altitude compensating capability; however, the aerospike geometry also presents an additional advantageous feature that is not generally recognized and acknowledged. Because most of the delivered thrust of the aerospike nozzle results from the upstream section of the spike, the nozzle can be truncated significantly from the theoretically optimum shape with little decrease in performance. Thus, truncated aerospike nozzles can be less than 25% the length of a conventional bell nozzle with the same performance level.⁴

On a small spacecraft, replacing a high-expansion ratio bell nozzle with an aerospike would significantly increase the volumetric efficiency of the configuration. This feature offers the possibility to provide significant savings in performance and overall system weight for in-space operations. Testing conducted by Bui et al.⁵ (NASA, 2005) concluded that switching to a comparable aerospike nozzle can result in mass savings of greater than 8%.

To date, aerospike nozzles have not been seriously considered for small satellite (*SmallSat*) propulsion systems due to the complexity of the plug systems support structures, and the associated manufacturing difficulties that do not scale well to small sizes. Furthermore, due to the relatively small annular throat gap and associated viscous boundary layer heating, for a given thrust level aerospike nozzles experience significantly higher heating levels than do conventional nozzles. The ability to manage this excess heating is exacerbated at small scales. Using conventional materials, *SmallSat*-scale aerospike nozzles would require complex external cooling schemes or otherwise experience limited operating lifetimes.

Fortunately, the emergence of 3-D metallic printing for refractory metals like tungsten, niobium, molybdenum, and rhenium offers a potential breakthrough that may allow the advantages of the aerospike nozzle to be realized for *SmallSat* operations. These refractory materials have been traditionally used in applications where their exceptional heat and wear resistance are required. Incentivized by the recent boom in additive manufacturing, there has been a growing interest in 3-D printing of refractory metals with for aerospace, medicine, nuclear power, and other general industrial applications.

Traditionally, high temperature refractory materials have not been 3-D print capable due to the difficulty of turning these metals into spherical-powders that are compatible with modern laser sintering methods. Recently, several companies in Germany, the United States, Japan and other countries have perfected core technologies that overcome the problem of turning refractory metals into 3-D printing materials. The refractory metal spherical powders for 3-D printing are now available in bulk, and are ready to be applied in the key components of aerospace industry.⁶

II. Test Article Design

In order to assess the feasibility and advantages of 3-D printing aerospike nozzles for *SmallSat* propulsion applications, a series of experiments were conducted using a legacy near-flight weight small scale hybrid rocket system with a nominal thrust level that was variable from 10-25 N, depending on the oxidizer feed pressure. The hybrid thruster for this testing campaign used gaseous oxygen (*GOX*) and 3-D printed acrylonitrile butadiene styrene (*ABS*) as propellants. Prior to this test series, the legacy motor had been successfully fired more than 100 times, and was well characterized. This test series compared the system performances using both fixed-geometry low (2.06:1) and higher (8.5:1) expansion ratio nozzles, against the same system retrofitted to use the higher (8.5:1) expansion ratio aerospike nozzle.

A. Thrust Chamber

Figure 3 presents a 2-D schematic and photograph of the disassembled motor. Depicted are the major components; *i) graphite nozzle, ii) nozzle retention cap, iii) motor case, iv) 3-D printed fuel grain with embedded electrodes, v) insulating phenolic liner, vi) chamber pressure fitting, and vii) single-port injector cap.* The 38-mm diameter thrust chamber is constructed from 6061-T6 high-temperature aluminum, and was procured commercially from Cesaroni Inc.[‡] Generally, two motor case lengths are available; a 1-G configuration that accepted a fuel grain of length up to 6.85 cm, and a 2-G configuration that accepted a longer fuel grain with length of up to 12.69 cm.

[‡] Anon., "Cesaroni Pro-X, A Better Way to Fly, Pro 38® hardware," <http://pro38.com/products/pro38/pro38.php>, [Retrieved 5 January, 2019].

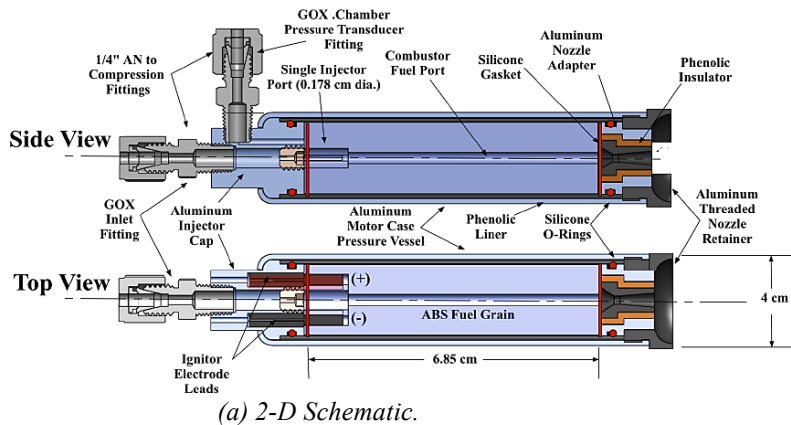


Figure 3. Test Article Thruster Assembly.

B. Nozzle Configurations

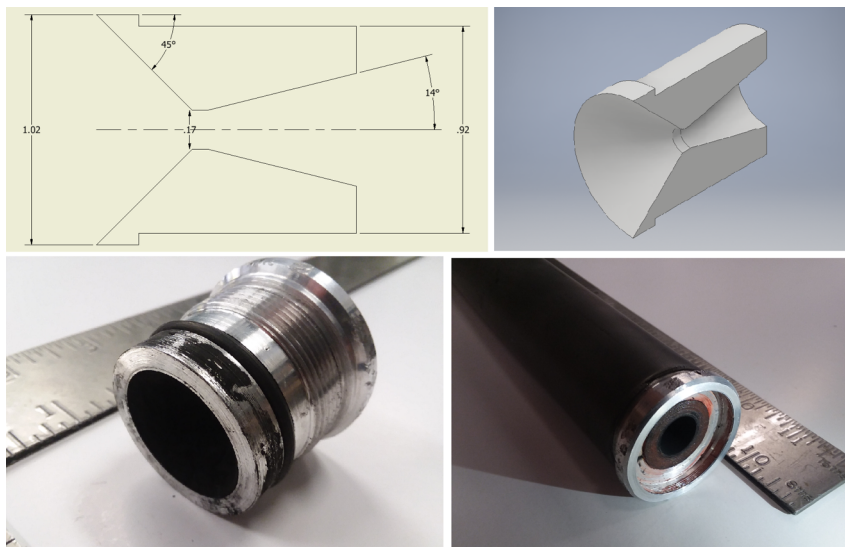


Figure 4. Conventional Conical Nozzle Design Schematic.

desired expansion ratio, and was calculated using the methods of Lee and Thompson.⁷ The contour of Ref. [7] assures that the flow along the nozzle spike will remain nearly isentropic and free of strong shock waves, even for highly over-expanded flow conditions. The geometry upstream of the throat can be more arbitrary. As long as a convergence on the nozzle throat produces choked flow, the nozzle will function. In an effort to reduce the stagnation area on the front end of the central spike and minimize heating, an aerodynamic Von Karman-type of ogive profile was chosen for the upstream contour. This profile belongs to a series of functions known as Haack series.⁸

Like the conical nozzle, the original design was conventionally fabricated, and featured a graphite sleeve to withstand the heating loads. Clockwise from the top left, Figure 5 depicts; i) graphite spike assembly and aluminum end piece, ii) CNC fabricated cantilevered spike contour, iii) full assembly CAD view, iv) picture of final assembly, v) stainless steel support arms, and vi) the graphite spike assembly. Figure 6 shows the aerospike nozzle assembly integrated with Cesaroni motor thrust chamber.

Later the design of Figure 5 was reproduced using Direct Metal Laser Sintering (DMLS) capability at the NASA Marshall Space Flight Center. Manufacturing was funded under a cooperative agreement between NASA and USU, with the part being built as a "ride-along" using spare build volume during the printing of another component for NASA Space Launch System. Nozzles printed from refractory metals was not an option within the budget constraints of the current study. Metals currently available at MSFC for 3-D printing purposes include tungsten, which possesses the highest known melting point of any metal, and Inconel 718, a nickel-chromium super-alloy known for its high-strength at high temperatures. Both of these metals are available in powdered form, a necessary for their utilization

Figure 4 depicts the conical nozzle assembly. Pictured, clockwise from the top left are i) the 8.5:1 nozzle contour, ii) a 3-D CAD model of the nozzle insert, iii) the nozzle retainer assembly, and iv) the nozzle assembly integrated onto the hybrid motor case. The fixed geometry nozzles were conventionally manufactured, and featured a graphite sleeve designed to withstand the heating loads with minimal erosion during the test firings.

Figure 5 shows the original design for the aerospike nozzle assembly. The spike contour downstream of the nozzle throat is ideally determined by the

through additive manufacturing. Inconel prints typically take 1-2 days to complete. Due to the high melting point tungsten prints require significantly more energy, and depending on the size of the print can take more than a week to complete. Thus, due to the experimental nature and higher programmatic risk of this campaign, Inconel was selected over Tungsten as a cost and time saving measure.

The entire assembly including threads, center spike, and mounting threads was printed 718-Inconel using an EOS-*M290* DMLS powder bed machine.⁹ The printed threads were designed to directly interface the nozzle assembly to the Cesaroni motor case. Figure 7 shows the 3-D Aerospike Nozzle Assembly printed as a single monolithic piece. The printed Inconel-718 piece was bonded to the nozzle retaining cap using high temperature RTV adhesive.

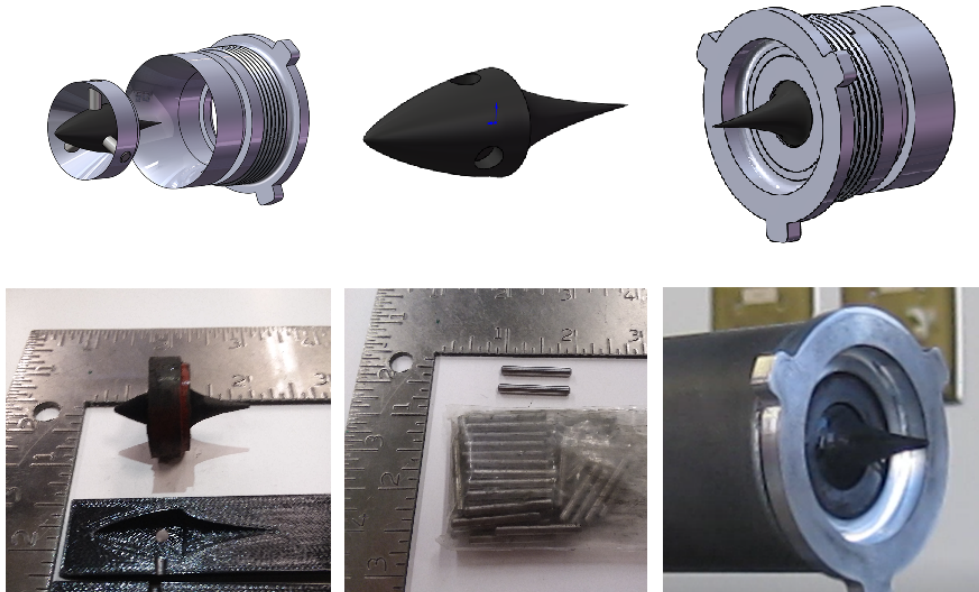


Figure 5. Design of Graphite-Sleeve Aerospike Nozzle.

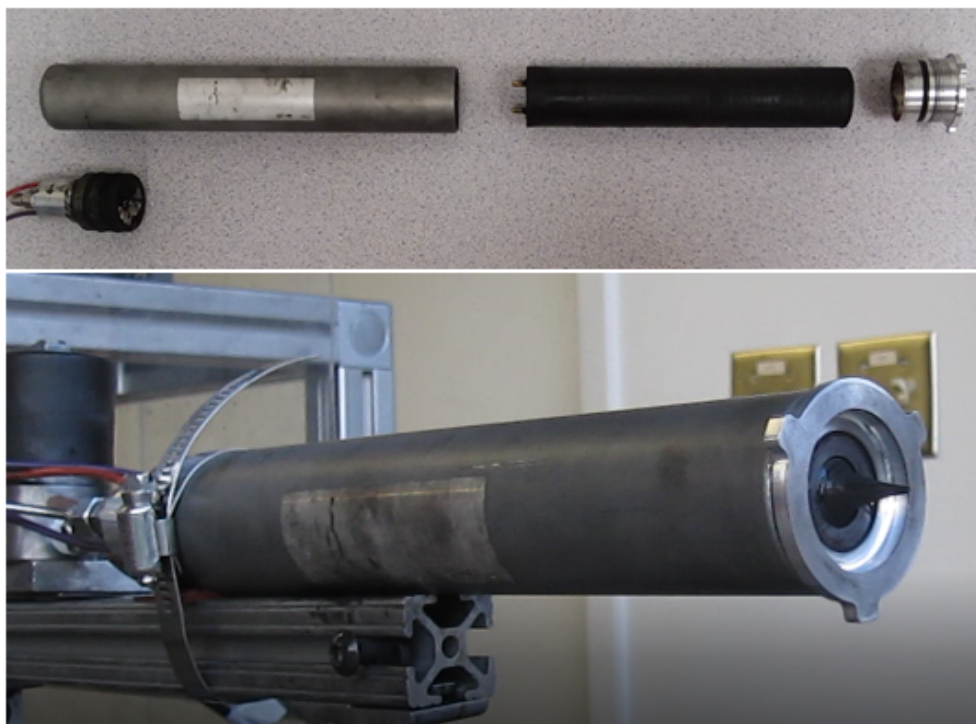


Figure 6. Aerospike Nozzle Assembly Integrated with Hybrid Motor Thrust Chamber.

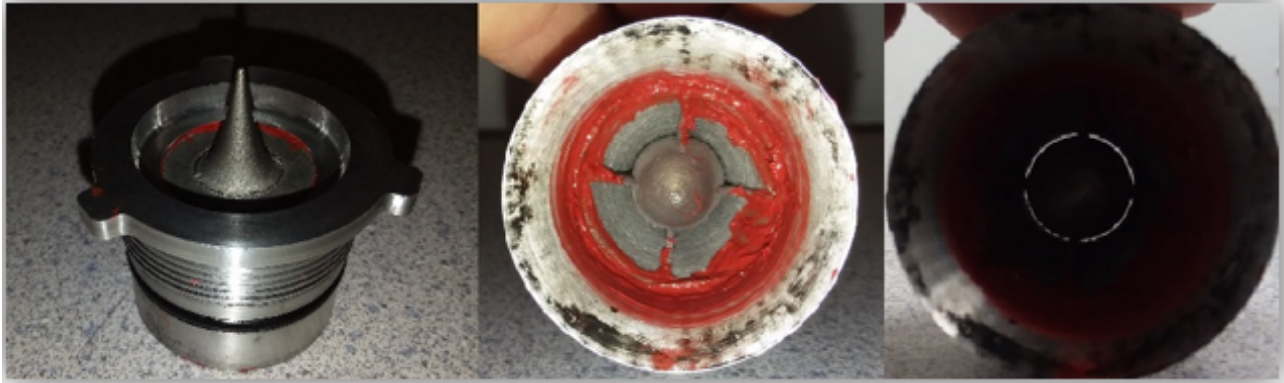


Figure 7. 3-D Printed One-Piece 718-Inconel Aerospike Nozzle and Retainer.

C. Fuel Grains.

The printed fuel grains were fabricated using a Stratasys Dimension 1200-ES® fused deposition model (FDM) printer.[§] Whitmore, et al (2016)¹⁰ investigated multiple commercially available 3-D printer feedstocks, and determined that ABSplus-340® feed-stock** exhibited to best overall arc-ignition and burn-performance characteristics. Currently, work is on-going to develop "designer" feed-stock plastic alloys that optimize the performance for propulsion applications.¹¹ Conservatively, in order to ensure adequate performance and operating characteristics for this testing campaign, all fuel grains were printed using Stratasys ABSplus-340® feed-stock.

D. Ignition System.

Motor ignition relies on the patented arc-ignition system developed at Utah State University by Whitmore (2015),¹² and Whitmore et. al (2015).¹³ The fuel grains used for this test series are based a

standardized design developed at the USU Propulsion Research laboratory. Figure 8 shows the pre-combustion chamber design that features two impingement shelves intended to trap and mix the injected oxidizer with the pyrolyzed fuel. Two electrodes, insulated by industry standard ESC-connectors,^{††} are embedded into the top face of the fuel grain. Wires are routed from the electrodes to small gaps located on the impingement shelves. The wires are insulated by printed circular sots that insert into the electrode wire gaps. The conducting paths terminate facing each other, flush with the combustion port surface, and exposed to the interior of the combustion chamber.

When an electrostatic potential is placed across the electrodes, electricity flows through a pre-existing surface arc-track, resulting in pyrolysis and ignition as soon as oxidizer flow is initiated. Typically, the arc-track is pre-set by doping the

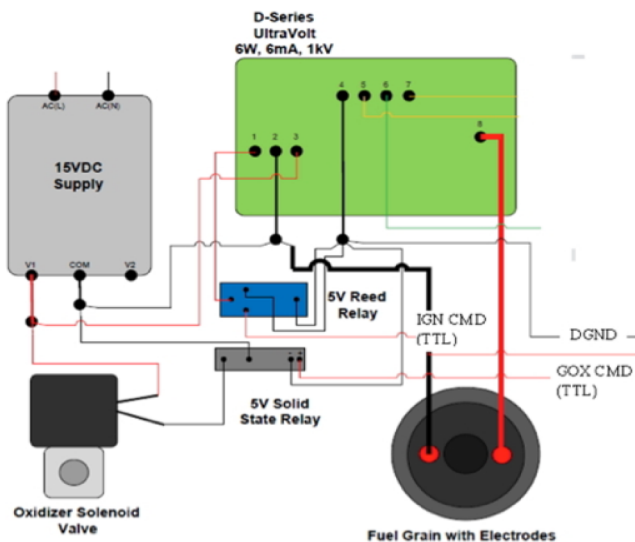


Figure 8. Ignition System Electronic Schematic.

[§] Anon., "Dimension 1200ES, Large, Durable Parts, <http://www.stratasys.com/3-D-printers/design-series/dimension-1200es>, [Retrieved 25 Jul. 2016].

** Anon., "ABSplus Spec Sheet," <http://usglobalimages.stratasys.com/Main/Secure/Material%20Specs%20MS/Fortus-Material-Specs/Fortus-MS-ABSplus-01-13-web.pdf>, [Retrieved 25 Jul. 2016].

†† Anon., "Motor to ESC Connectors," <https://www.motionrc.com/collections/motor-to-esc-connectors>, [Retrieved 6 June 2017].

surface with graphite powder. Once a surface arc-path has been set, graphite doping is no longer required. The fuel grain terminals are connected to mating connectors on the injector cap, and the phenolic liner is placed on the outside of the fuel grain. The entire assembly slides into the motor case.

The ignition system power processing unit (PPU) is based on the UltraVolt® D-series line of high-voltage power supplies (HVPS).^{‡‡} Figure 9 shows the layout of the arc-ignition system. This HVPS provides the inductive ignition spark that pyrolyzes sufficient ABS material to seed combustion. The D-series HVPS units take a 15-volt DC input and provide a current-limited (7.5 mA) high voltage output -- up to 1000 V or 6 Watts total output. Previous experience with this ignition system has demonstrated that ignition can be reliably achieved using as little as 3 watts. Depending on the impedance on the arc path between the ignitor electrodes, the dissipated voltage typically varies between 10 and 400 volts. Total energy of ignition is typically less than 3 Joules.

III. Laboratory Test Apparatus

The same instrumentation system was used for both the ambient pressure tests performed at Utah State and the Vacuum tests performed at NASA MSFC. However, due to the different safety demands of both organizations, different oxidizer delivery systems were used for the USU-based and MSFC-based testing campaigns. This section describes the two test systems in detail.

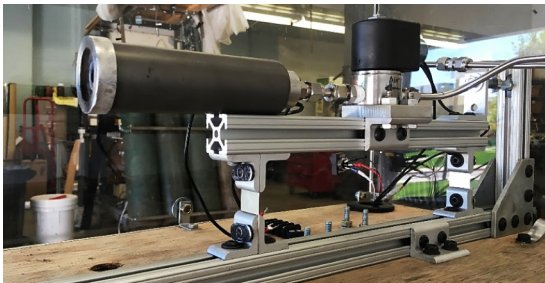


Figure 9. Thrust Chamber Mounted to Load-Balance Test Sled.

E. Experimental Apparatus for Ambient Test Conditions

All ambient tests were performed in the Propulsion Research Laboratory, located at Utah State University. Depicted is the fully assembled thrust chamber mounted to the test-sled. Figure 9 shows the flight weight motor assembled and ready for testing, and mounted to the test load balance. Figure 10 shows the piping and instrumentation diagram (P&ID) and the USU ambient test systems. Figure 11 shows the detailed layout of the test instrumentation deck. The instrumentation deck was designed to be portable so it could be used for both for the ambient pressure tests at USU and the vacuum tests at MSFC.

Test stand measurements include venturi-based GOX massflow measurements, load-cell based thrust measurements, chamber pressure, and multiple temperature readings at various points along the flow path. The differential venturi pressure transducer was installed to increase the accuracy of the sensed pressure drops. The thrust-stand support members allow bending along the direction of thrust to prevent them from interfering with the measured load. The entire test assembly is made using commercially available T-slot^{§§} extruded-aluminum components.

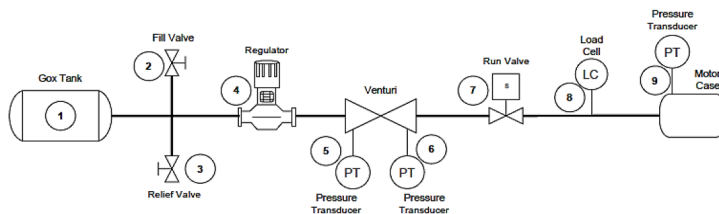


Figure 10. Piping and Instrumentation Diagram of the Ambient Test Apparatus, Logan UT.

Directly aft of the thrust chamber lies the solenoid actuated GOX run-valve. The solenoid flow valve is actuated via a digital out command from the instrumentation. The National Instruments (NI) USB-6002 is shown in Fig. 8 as the “Ignition Control” because it sends digital signals to the solenoid valve via the solid-state relay and HVPS using LabView as the controller. The

24V power supply is used to supply power to the solenoid valve and HVPS; whereas, the 15V power supply is used to power the transducers. The thermocouples, venturi inlet, differential, and chamber pressure transducers, along with the load cell have their signals conditioned using National Instruments Data Acquisition (DAQ) units.

^{‡‡} Anon., “High Power 8C-30C Series, Single Output High Voltage DC/DC Modules,” UltraVolt, Inc., http://www.ultravolt.com/uv_docs/HP8C-30CDS.pdf, [Retrieved 9 December 2016].

^{§§} Anon., “T-Slotted Aluminum Extrusions,” <http://www.tslots.com/>, [Retrieved 25 Jul. 2016].

The HVPS provides low voltage signals that are proportional to the output current and high-voltage for tracking the unit operation. The high voltage output is initiated by a commanded TTL-level input signal through the NI USB 6002. Two separate commands are required to initiate the ignition sequence. For this test series, the firing sequence that ensured reliable ignition sends the spark TTL command 250 ms - 500 ms before the GOX-valve open command. The spark potential then continued for 250 ms - 500 ms after the GOX-valve has opened.

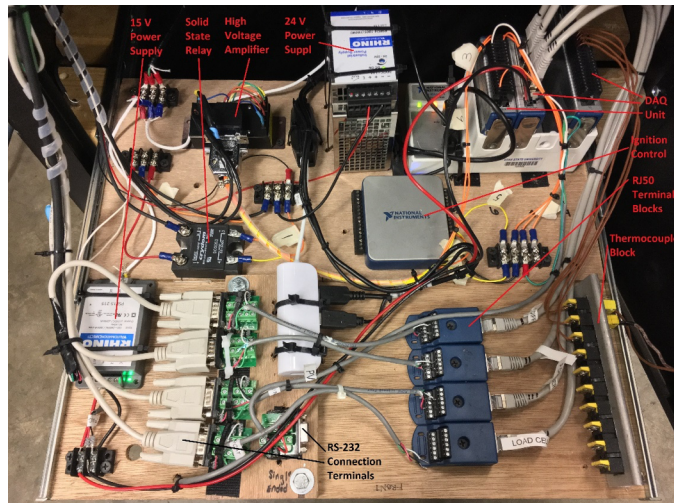


Figure 11. Instrumentation Deck Layout.

instrumentation deck. The primary difference for the vacuum tests was the oxidizer pressurization and delivery system, as mandated by NASA safety rules. The vacuum chamber systems were also unique to the MSFC tests. These systems are described in the following sub-sections. Figure 12 presents the Piping and Instrumentation Diagram of the Vacuum Test Systems.

Oxidizer Pressurization System

The pressurization system is responsible for regulating the oxidizer feed to the thruster injector pressure at the desired level. The three-stage system consists of a low pressure (125 psig) air-feed that provides the dome-regulation a high-pressure (max 1400 psig) nitrogen gas (GN2) system, that in turn provides the dome control input for the GOX feed system regulator. The three-stage system is necessary to allow the regulated pressure to be controlled remotely with the test cell blast-door closed.

- The facility 125 PSIG High Purity Air Supply line was used for actuating the remote valves and is contained in a completely different set of lines from the GN2 propellant pressurization system.
- Regulators IP-201 and HOR-203 supply the low-pressure air dome control for the second stage dome-loaded regulator DLR-104.
- Regulator DLR-104 supplies the intermediate pressure (max 1400 psig) GN2-dome control input to GOX dome-loaded regulator DLR-7.
- A GN2 purge line is tee'd into the GOX feed line and flow is initiated via HOV-103.
- Dual-redundant check valves CV-100 and CV-101 downstream of GN2 manual valve HOV-103 preclude the high-pressure GOX (max 2400 psig) flow from entering the GN2 intermediate-stage pressurization system.
- Check-valve CV-300 prevents GN2 from entering the high-purity air system.

Oxidizer Delivery System

The oxidizer delivery system is responsible for containing and delivering gaseous oxygen at the desired pressure level to the thruster injector cap. The GOX rate of flow is measured by a custom built and calibrated Venturi flow meter VEN-12 and associated pressure transducers PT-401 and DPT-402. The GOX storage tank is isolated from the thruster with SOV-13, and manual valves HOV-6 and HOV-2. The chamber pressure transducer PT-403 is installed with 1/8" stainless steel line into the motor cap and measures the motor head-end combustion pressure. When the hand

F. Experimental Apparatus for Vacuum Test Conditions

All vacuum tests were performed in Test Cell C the Chemical Synthesis and Testing Laboratory at NASA Marshall Space Flight Center (MSFC). Prior to testing a full safety assessment (SA) was performed, and hazards were identified and mitigated. The SA was performed to demonstrate the ability to safely perform the proposed testing and to ensure compliance with NASA, OSHA, and national consensus standards.

The vacuum test apparatus used as much of the USU-based test components as possible including the thrust load-balance and the

operated isolation valves (HOV-2, HOV-6) are opened, two additional remotely operated valves ROV-10 and SOV-13 isolate the GOX feed from the motor combustion chamber. The upstream pneumatic valve ROV-10 allows the system to be remotely pressurized prior to initiating the run-sequence via SOV-13.

The remotely operated solenoid valve SOV-13 initiates the oxidizer flow into the thrust chamber and serves as the "run valve" for the system. The Venturi pressure measurement via PT-401 is used to judge that the system is fully pressurized and ready for opening of the GOX run valve. The third stage dome-loaded regulator DLR-7 sets the desired inlet pressure to the thruster injector.

The output from DLR-7 is controlled by the dome-inputs from DLR-104 and the output difference between IP-201 and HOR-203. The firing-systems control software sets the commanded current input to IP-201.

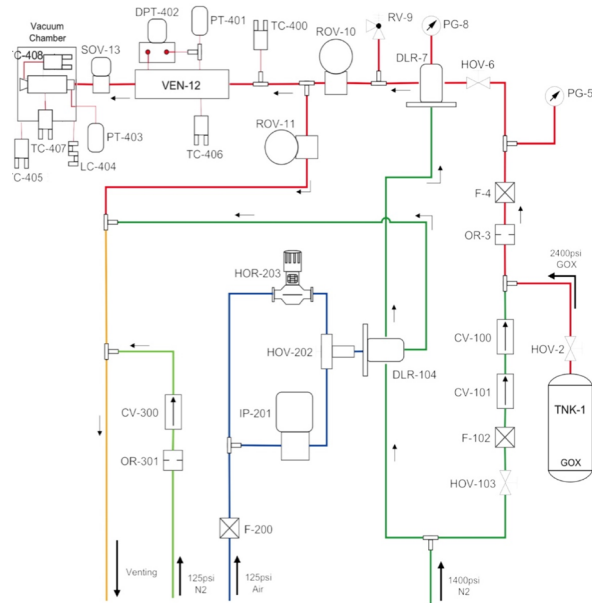


Figure 12. P&ID of MSFC Pressure, Oxygen Delivery, and Vacuum Test System.

Vacuum Chamber Altitude Simulation System

The altitude system consists of an altitude chamber, roughly 4.5 ft³ in volume, evacuated by a rotary vacuum pump, with the pump discharging outside of the building into a stainless steel drum. The chamber can be purged with air via HOV-ROV-11 from the facility 125 PSIG High Purity Air Supply or GN2 via either ROV-11 or HOV-103. ROV-11 purges the system downstream of ROV-10. HOV-103 purges any residual GOX that may lie between the GOX inlet and ROV-10. The vacuum pump has been serviced to safely pump GOX and is filled with perfluoropolyether oil.

Vacuum Chamber Thruster Performance Measurement Systems

The thruster performance measurement system is wholly contained within the altitude chamber. A single Omega LCCA 25 lbf load cell LC-404 was used to measure longitudinal force generated by the motor. Thermocouples are attached to the Venturi (TC-406), motor thrust chamber (TC-407), and nozzle exit plane (TC-408) and sense critical motor temperatures. TC-406 is used to calculate the flow density in the compressible GOX mass flow calculations. A motor case temperature exceeding 250 deg. C and a nozzle exit plane temperature exceeding 500 deg. C triggers a motor firing abort. A thermocouple (TC-405) was also attached to the aft wall of the vacuum chamber. A chamber wall temperature exceeding 800 deg. C triggers a motor firing abort. Locations of these sensors are shown on the P&ID of Figure 9. The thrust stand load measurements were calibrated using the installed configuration with the pressure lines loaded at full pressure levels. Figure 13 shows the thrust chamber mounted on the test sled and inside of the vacuum chamber.

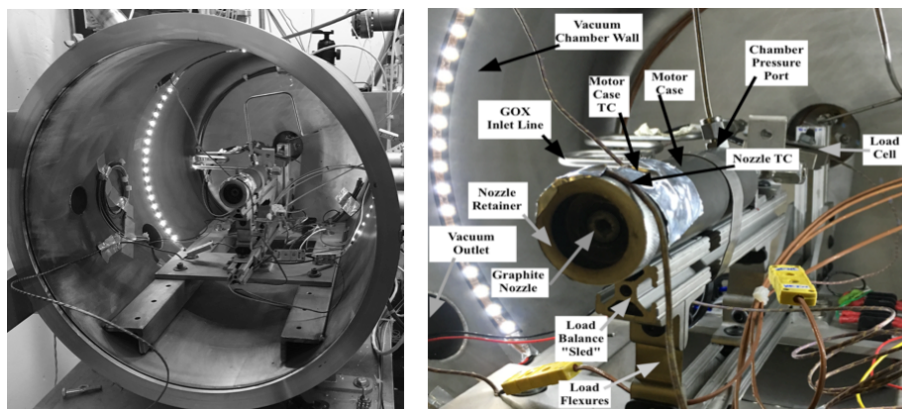


Figure 13. Thruster Mounted in Vacuum Chamber with Labeled Features.

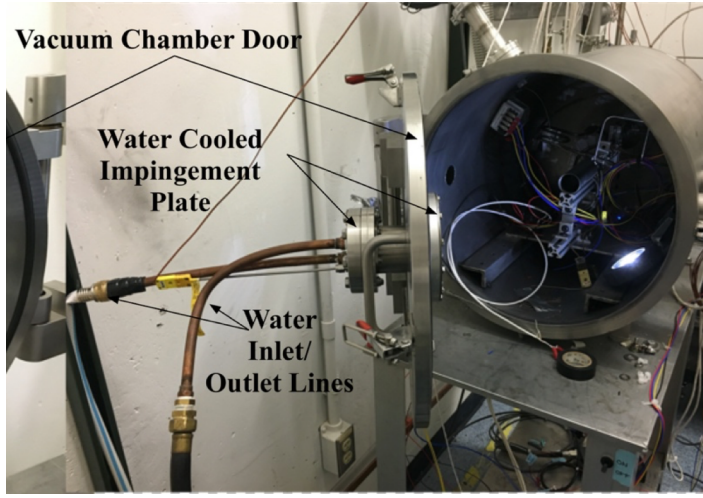


Figure 14. Vacuum Chamber Cooling Apparatus.

Vacuum Chamber Thermal Management System

As will be shown later in the *Results and Discussion Section*, the output massflow was approximately 10 grams/second, with a resulting enthalpy output of 80 kW being pumped into the vacuum chamber during hot firings. This large power input resulted in substantial chamber heating, affecting the test results. As a thermal management system, a custom water cooled impingement plate was design and installed into the view port of the chamber door. The water flow was managed so as to keep the impingement plate surface temperature below 400 deg. C. Figure 14 shows the impingement plate mounted to the vacuum chamber entry door.

IV. Test and Analysis

Experimental tests of both the fixed-geometry and aerospike nozzles were performed at the Utah State University's (USU) Campus Propulsion Research Laboratory test cell, and at the NASA Marshall Space Flight Center's Chemical Synthesis and Testing Laboratory. The USU-based tests were all performed under ambient conditions, whereas the MSFC tests were performed under simulated vacuum conditions using a small vacuum chamber. Whitmore and Bulcher,¹⁴ and Whitmore¹⁵ describe the analytical methods, test apparatus, instrumentation, test procedures, and analysis methods used to derive the presented data in much fuller detail. This section summarizes the major conclusions of this testing campaign. Complete, detailed results from this testing campaign, including time histories of each test, and tabulations of each test result are presented by Armstrong (2018).¹⁶

G. Analytical Methods

Modeling the Shock Wave in the Over-Expanded Nozzle

The conventional conical nozzle with the 8.5:1 expansion ratio was designed to be over-expanded for the operating chamber pressure and the ambient test conditions at the Logan Utah test cell, approximately 1,400 meters (4700 ft.) above mean sea level. The design resulted in an embedded shockwave downstream of the nozzle throat. The expected shock wave position w was calculated using the method developed by Anderson.¹⁷ According to Anderson's one dimensional flow model, for a given value of the parameter

$$\frac{P_0 A^*}{p_e A_e}, \quad (1)$$

the exit Mach number M_e is calculated explicitly as

$$M_e = \sqrt{-\frac{1}{(\gamma-1)} + \sqrt{\left(\frac{1}{(\gamma-1)}\right)^2 + \frac{2}{(\gamma-1)} \left(\frac{2}{\gamma+1}\right)^{\frac{\gamma+1}{\gamma-1}} \left(\frac{P_0 A^*}{p_e A_e}\right)^2}} \quad (2)$$

In Eq. 2 the parameter P_0 is the combustion chamber stagnation pressure, A^* is the nozzle throat area, p_e is the nozzle exit pressure, and A_e is the nozzle exit area, and γ is the ratio of specific heats at constant pressure and volume. In the

presence of an embedded shock wave there is a stagnation pressure loss, and the stagnation pressure ratio across the shock wave is

$$\frac{P_{0_2}}{P_{0_1}} = \frac{P_e}{P_{0_1}} \left[1 + \frac{(\gamma-1)}{2} M_e^2 \right]^{\frac{\gamma}{\gamma-1}} \quad (3)$$

The Mach number ahead of the shockwave, M_1 , was calculated using Newton's method to iteratively solve the stagnation pressure/Mach equation,

$$\frac{P_{0_2}}{P_{0_1}} = \frac{2}{(\gamma+1) \left(\gamma M_1^2 - \frac{(\gamma-1)}{2} \right)^{\frac{1}{\gamma}}} \left(\frac{\left[\frac{(\gamma+1)}{2} M_1^2 \right]^2}{\left(1 + \frac{\gamma-1}{2} M_1^2 \right)} \right)^{\frac{\gamma}{\gamma-1}} \quad (4)$$

Finally, Mach number ahead of the shockwave is used to calculate the area A_1 at which the shockwave forms aft of the throat,

$$\frac{A_1}{A^*} = \frac{1}{M_1} \left[\left(\frac{2}{\gamma+1} \right) \left(1 + \frac{(\gamma-1)}{2} M_1^2 \right) \right]^{\frac{\gamma+1}{2(\gamma-1)}} \quad (5)$$

The location of the expected shockwave is found using the nozzle geometry and the area found by Eq. (5).

Computational Sequence for Massflow, Fuel Regression Rates, Instantaneous O/F, and Equivalence Ratios

The compressible venturi massflow equations are derived from material presented by Anderson [17] (Chapter 3, pp. 65-121). For the operating massflow levels the venturi inlets exhibited sufficient flow velocity the upstream stagnation pressure must be calculated from the venturi upstream and throat static pressure readings. The entering stagnation pressure is calculated from the sensed inlet P_1 and throat P_2 absolute pressure levels, and the venturi inlet A_1 and throat flow areas A_2

$$P_0 = \frac{\left[\left(\frac{A_1}{A_2} \right)^2 \cdot (P_1)^{\frac{\gamma+1}{\gamma}} - (P_2)^{\frac{\gamma+1}{\gamma}} \right]}{\left[\left(\frac{A_1}{A_2} \right)^2 \cdot (P_1)^{\frac{2}{\gamma}} - (P_2)^{\frac{2}{\gamma}} \right]} \quad (6)$$

Once the true inlet stagnation pressure is calculated, then the achieved massflow is calculated using the un-choked compressible massflow equation

$$\dot{m}_{ox} = C_d \cdot A_1 \cdot P_0 \sqrt{\left(\frac{2\gamma}{\gamma-1} \right) \frac{1}{R_g \cdot T} \left[\left(\frac{P_1}{P_0} \right)^{\frac{2}{\gamma}} - \left(\frac{P_1}{P_0} \right)^{\frac{\gamma+1}{\gamma}} \right]} \quad (7)$$

The calculation of Eq. (2) requires a temperature measurement T , and this value was measured using a thermocouple installed on the venturi flow block. The flow discharge coefficient C_d accounts for frictional flow losses. Both venturi flow meters were calibrated using cold flow tests that captured the total mass passed through the system. The discharge coefficients were estimated by dividing the measured total mass through the system against the calculation of Eq. (5) (assuming $C_d=1$) integrated over the burn duration.

Although the inline GOX venturi measures the oxidizer mass flow in real-time, the test stand could not measure real-time fuel mass flow. Thus, for this testing campaign the "instantaneous" fuel mass flow rates were calculated as the difference between the measured nozzle exit and oxidizer mass flow rates,

$$\dot{m}_{fuel} = \dot{m}_{total} - \dot{m}_{ox} \quad (8)$$

For all runs the regulator pressure and injector port diameter were pre-set to choke the injector flow and ensure a constant oxidizer mass flow. Choking the injector flow ensured very low run-to-run variability in the oxidizer massflow rate, and significantly reduced the risk of incurring injector-feed coupling instabilities during combustion. The nozzle exit mass flow time history was calculated from the measured chamber pressure time history P_0 , nozzle throat area A^* , and the exhaust gas properties (flame temperature T_0 , ratio of specific heat γ , molecular weight M_w , and specific gas constant R_g) using the 1-dimensional choking mass flow equation, (Anderson [16], Chapt. 4).

$$\dot{m}_{total} = A^* \cdot P_0 \cdot \sqrt{\frac{\gamma}{R_g \cdot T_0} \cdot \left(\frac{2}{\gamma+1}\right)^{\frac{\gamma+1}{\gamma-1}}} \quad (9)$$

The mean longitudinal fuel regression rate was calculated from the fuel mass flow by,

$$\dot{r}_L = \frac{\dot{m}_{fuel}}{2\pi \cdot \rho_{fuel} \cdot r_L \cdot L} \quad (10)$$

Integrating Eq. (10) from the initial condition to the current time frames solves for the longitudinal mean of the instantaneous fuel port radius.

$$r_L(t) = \sqrt{r_0^2 + \frac{1}{\pi \cdot \rho_{fuel} \cdot L} \int_0^t \dot{m}_{fuel} dt} \quad (11)$$

The instantaneous cross sectional area of the fuel port is,

$$A_c(t) = \pi \cdot r_L^2(t) = \pi \cdot r_0^2 + \frac{\Delta M_{fuel}}{\rho_{fuel} \cdot L_{port}} \quad (12)$$

The instantaneous oxidizer mass flux, total mass flux, O/F ratio, and equivalence ratio are estimated by:

$$\left[\begin{array}{l} \bar{G}_{ox} = \frac{\dot{m}_{ox}}{A_c(t)} \\ \bar{G}_{total} = \frac{\dot{m}_{total}}{A_c(t)} \\ O/F = \frac{\dot{m}_{ox}}{\dot{m}_{total} - \dot{m}_{ox}} \\ \Phi = \frac{O/F_{stoich}}{O/F_{actual}} \end{array} \right] \quad (13)$$

For each data point in the burn time history, two-dimensional tables of thermodynamic and transport properties were interpolated to calculate the gas constant R_g , ratio of specific heats γ , and flame temperature T_0 . The table of equilibrium properties of the GOX/ABS exhaust plume were developed by Whitmore, et. al (2013)¹⁸ with measured



Figure 15. Cone Nozzle Time Lapse Burn Images.

downwards decreases the calculated fuel mass consumption. The fuel massflow calculation starts with an assumed combustion efficiency of $\eta^* = 0.90$. The calculations of Equations (3-10) were iterated, adjusting η^* until the calculated fuel mass equals the measured mass and total consumed propellant O/F ($\Delta M_{ox}/\Delta M_{fuel}$) within a prescribed level of accuracy ($\frac{1}{2}\%$). The approximate stoichiometric O/F ratio for GOX/ABS is 2.67.

Once the total massflow, exit plane Mach number, and stagnation temperature, and stagnation pressure were calculated using the above procedure, then the remainder of the motor performance parameters could be calculated. Calculated performance parameters for the off-design configuration include thrust coefficient C_F , effective exhaust c_e , and specific impulse I_{sp} . Similarly, the "sensed" performance parameters for the aerospike and conical nozzles were calculated from the measured thrust level and using the total massflow calculation from Eq. (9), based on the sensed chamber pressure values.

H. Effect of Fuel Grain Length on Motor Performance and Burn Temperature.

As described in the previous section, for the test motor two configurations are available; a "1-G" configuration that accepts a fuel grain of length up to 6.85 cm, and a "2-G" configuration that accepts a longer fuel grain with length of up to 12.69 cm. For the motor size and operating chamber pressure, the choice of motor length significantly influenced the oxidizer-to-fuel ratio (O/F) for the system; with the shorter motor producing O/F ratios varying from 1.5 to slightly greater than 3. The longer motor resulted in significantly lower O/F ratios with values varying from approximately 0.4 to slightly less than 1.0.

This low O/F had several effects, notably lowering combustion flame temperature, and producing a large percentage of sooty particulates in the rocket plume. All burns exhibited a negative O/F shift as a function of burn lifetime. Detailed reasons for this negative shift, and a thermodynamic model describing the process are presented by Whitmore and Merkley (2016).²⁰ The fuel-rich behavior can be seen in the burn time history "slideshow" of Fig. 15. From top to bottom these images depict, i) GOX ignition, ii) Steady state flow with shock diamonds formed, iii) End of steady state flow, plume noticeably fuel rich, and iv) Motor cutoff. The total depicted burn duration is approximately 4 seconds.

chamber pressure P_0 , combustion efficiency η^* , and mean O/F ratio as independent look up variables for the tables. Reference [18] used NASA's industry standard chemical equilibrium code CEA code¹⁹ to perform the calculations.

Each fuel grain was burned multiple times to allow interim fuel mass consumption measurements between burns. The corresponding oxidizer mass consumed was calculated by integrating the venturi mass flow time history over the burn duration. The mean O/F ratio over the burn duration was estimated by dividing the consumed oxidizer mass by the consumed fuel mass. By adjusting η^* the flame temperature was scaled

$$T_{0_{actual}} = \eta^{*2} \cdot T_{0_{ideal}} \quad (14)$$

To adjust nozzle-exit massflow and the resulting consumed fuel massflow,

$$\Delta M_{fuel} = \int_0^t (\dot{m}_{total} - \dot{m}_{ox}) dt \quad (15)$$

Adjusting input combustion efficiency upwards has the effect of increasing the calculated fuel mass consumption, and

Assuming GOX and ABS as propellants, Figure 16 compares the operating O/F ranges of the test motor using the short and long fuel grains against theoretical calculations of the chamber combustion temperature T_0 , and 100% efficient characteristic velocity c^* as calculated using CEA, Ref. [19]. For these propellants the stoichiometric O/F ratio is approximately 2.0, with a best performance occurring at an O/F of approximately 1.5. Swapping from the short (1-G) to the long (2-G) motor lowers the performance by slightly greater than 10%. More significantly, this swap also lowers the flame temperature by more than 1200 °C. This reduction in flame temperature would significantly increase the operating lifetime of the aerospike nozzle, especially under vacuum conditions where passive convection is not available to cool the nozzle.

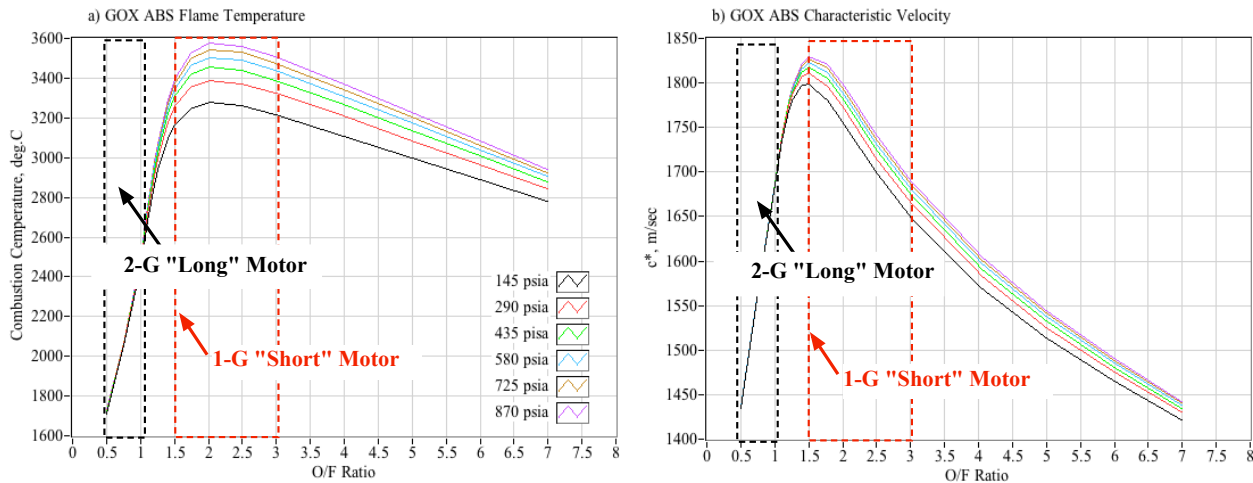


Figure 16. Comparing Flame Temperatures and Performance of Long (2-G) and Short (1-G) Fuel Grain Motors.

Figure 17 shows final state of the conventionally-manufactured carbon throat aerospike nozzle at the end of ambient testing. The spike and supports are entirely intact, with a slight erosion of the throat annulus. However, when the 3-D printed Inconel aerospike nozzle was first tested in the vacuum chamber using the shorter grain motor, the nozzle failed almost immediately upon reaching steady state operating conditions. Figure 18 shows this result. Depicted events/images are 1.) *Burn 27 motor start-up*, 2.) *Failure of support arm releases flow on one side*, 3.) *Nozzle remains glow white hot even after motor cut-off*, 4.) *State of nozzle after burn 25*, 5.) *State of nozzle after burn 26*, 6.) *State of nozzle after burn 27*, and 7.) *Molten Inconel residue on vacuum chamber wall*. The failure of the 3-D printed test article was caused by shearing of a cantilevered support arm that remained intact on the carbon aerospike tested dozens of times at USU.



Figure 17. Intact Carbon-Throat Aerospike at Completion of Ambient Testing.

When the short motor was swapped for the longer motor, the reprinted 3-D printed Inconel nozzle survived multiple vacuum burns with no failure issues. Thus, for the vacuum aerospike tests all of the reported data were obtained using the longer (2-G) motor. The reduced performance was accepted as a compromise to ensure the printed nozzle integrity for the duration of the testing campaign. The conventional nozzle tests were performed using both the short and long motor cases.

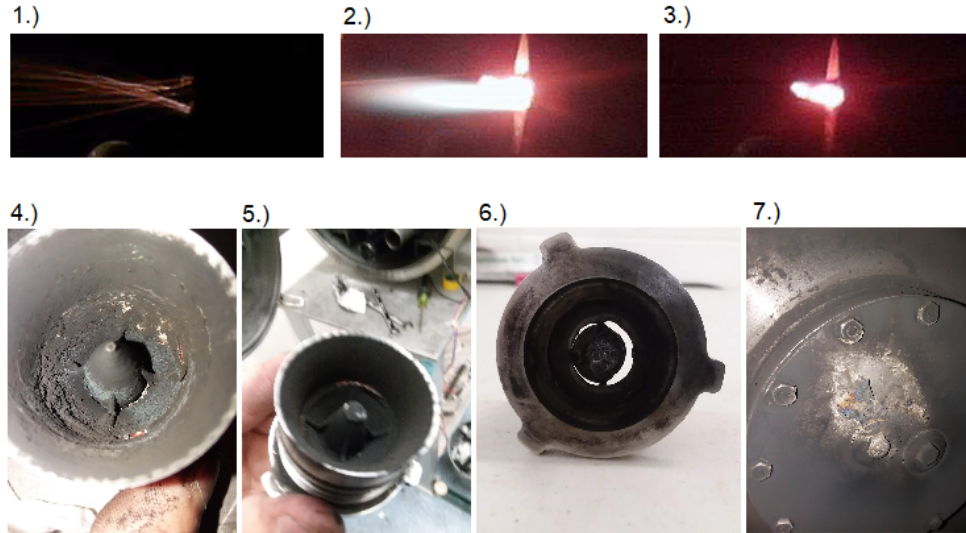
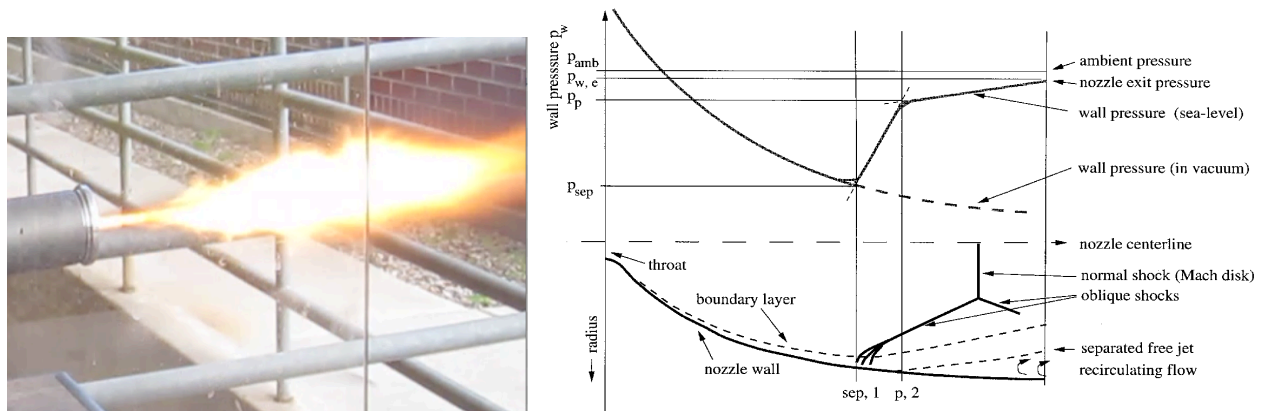


Figure 18. Thermal Failure of 3-D Printed Inconel Aerospike Nozzle.

I. Qualitative Test Results

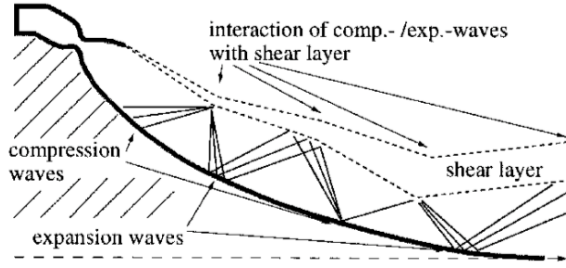
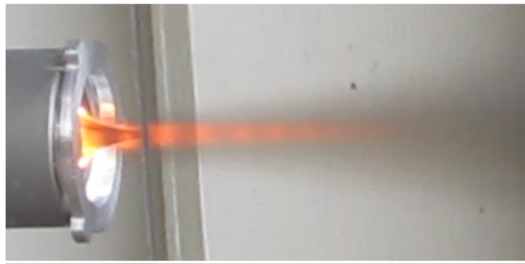
Figure 19 shows the over-expanded 8.5:1 conical nozzle being tested under ambient conditions at the at the USU Propulsion Research Laboratory. The top image (a) of this figure shows the "pinched" exit stream line that eventually breaks down to re-expand to the ambient pressure level. The bottom image (b) shows the theoretical wall pressure profile, and a general interpretation of the flow phenomenology. No external shock diamonds are visible in Figure 19, and this visual cue indicates that the flow external to the nozzle is subsonic. As depicted by Figure 19 (b), subsonic flow results from the flow downstream of the embedded internal shock wave or Mach disk. The depicted interpretation is based on the previously presented analytical shock-model from Ref. [17] and on discussions as presented by Hagemann, et. al.²¹ The ragged plume appearance is indicative of the nozzle's internal flow separation.



(a) Over-expanded Conical Nozzle Exit Plume. (b) Over-expanded Conical Nozzle Pressure Profile, and Flow Phenomenon Interpretation.

Figure 19. Typical Ambient Test of the 8.5:12 Fixed-Geometry Conical Nozzle.

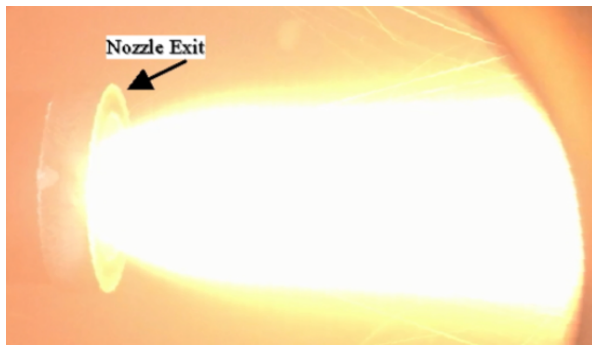
In contrast, Figure 20 shows the aerospike nozzle as tested under ambient conditions at the USU Propulsion Research Laboratory. Starting from top to bottom, Figure 20 depicts (a) the over-expanded aerospike nozzle plume, and (b) the theoretical interpretation of the observed flow phenomenon from Ref.[21]. The external shock diamonds and external boundary shear layer are clearly visible on Figure 15b, indicating a fully-started nozzle. Clearly, even though the aerospike nozzle is designed with an expansion ratio that is optimal for a significantly higher altitude, approximately 24,000 ft., the configuration is fully started at the operating altitude of the USU Propulsion Laboratory, approximately 1,400 meters (4700 ft.) above mean sea level.



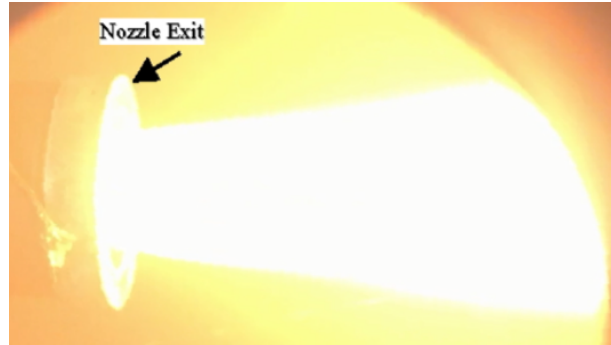
(a) Over-Expanded Aerospike Nozzle Exit Plume. (b) Over-Expanded Aerospike Nozzle Flow Phenomenon Interpretation.¹⁰

Figure 20. Ambient Test of the 8.5:1 Aerospike Nozzle.

Figure 21 shows additional plume images for the low (2.06:1) and high expansion ratio (8.5:1) conical nozzles during vacuum testing at the MSFC Chemical Synthesis Lab. Note that the low expansion ratio plume immediately splay out after leaving the nozzle exit, whereas the higher expansion ratio nozzle plume extends nearly straight aft with only a minor amount of expansion. This result indicates that the 8.5:1 nozzle is very nearly optimized for the test conditions achieved during the MSFC vacuum testing. Figure 22 presents a similar image for the Aerospike Nozzle obtained during vacuum testing. The test geometry was identical to that used to generate the image of Figure 14. The plume appearance is strikingly similar to that of the Higher expansion ratio conical nozzle, with the plume appearing to stream straight aft with only a minor expansion downstream of the aft end of the center spike. The resulting stream lines show that the plug design has fully compensated for the effects of altitude.



(a) 2.06:1 Conical Nozzle



(b) 8.5:1 Conical Nozzle

Figure 21. Exhaust Plume Images from Vacuum Tests of Low (2.06:1) and Near-Optimal (8.5:1) Conical Nozzles.

J. Quantitative Test Results

Multiple Test Burns were collected for the low and high expansion ratio conical nozzles and the aerospike nozzle under both ambient and vacuum test conditions. Figures 22 and 23 plot the resulting calculations for specific impulse (I_{sp}), with each data point plotted as a function of the mean O/F ratio over the burn duration. Figure 22 compares the nozzle performances for ambient conditions, and Figure 23 compares the performances for vacuum test conditions. Also plotted on Figure 23 are calculations from a 1-D embedded shock wave model of Ref. [17]. Figure 23 plots the predicted isentropic specific impulse values for the high expansion ratio nozzles.



Figure 22. Exhaust Plume Images from Vacuum Tests of 8.5:1 Expansion Ratio Aerospike Nozzle.

K. Discussion of Results

In Figures 21 and 22 the conical nozzle test results are as expected, with the low expansion ratio nozzle exhibiting superior performance at low altitude, and the higher expansion ratio nozzle exhibiting better performance under

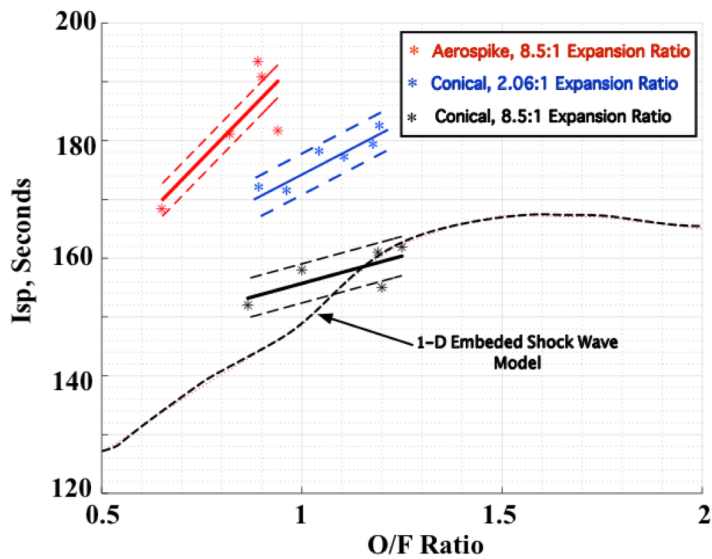


Figure 21. Conventional and Aerospike Nozzle Specific Impulse Comparisons for Ambient Test Conditions.

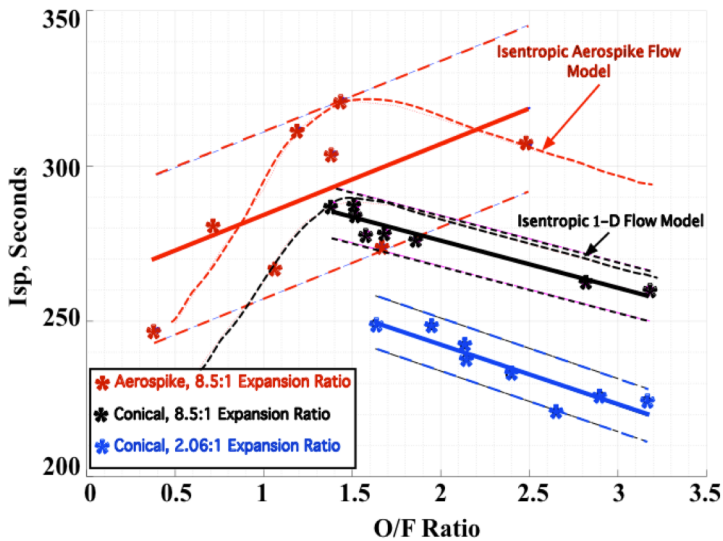


Figure 22. Conventional and Aerospike Nozzle Specific Impulse Comparisons, Vacuum Test Conditions.

recent innovation in the world of Additive Manufacturing, and offers the ability to manufacture parts of virtually any complexity of geometry without the need for any tooling. Tungsten has the highest melting temperature (3422 °C) of any metal in pure form. This temperature is more than 2000 °C higher than Inconel. Finally, Tungsten does not oxidize at high temperatures and would very likely allow the aero-spike motor to be operated erosion-free near stoichiometric conditions for an extended period without the need for active cooling.

vacuum conditions. However, for both ambient and vacuum data plots the motor with the aerospike nozzle exhibits the highest relative specific impulse level. This positive result comes in spite of the lowered c^* performance of the aerospike nozzle due to the lower O/F ratio of the longer motor used for the aerospike tests.^{***} Between each aerospike burn, some attempt was made to clean the nozzle annulus of deposited soot; however, the backed-on material was quite solid and difficult to remove.

The deposited burn material had a significant, unpredictable effect on the total annular throat area, and the higher scatter exhibited by the aerospike data in Figure 22 is likely due to soot deposits building up in the small nozzle throat. In spite of this shortcoming, the altitude compensating properties of the aerospike nozzle are well demonstrated by these data plots. Results indicate an average increase in I_{SP} of around 10-15 seconds is possible by switching from a bell nozzle to a similarly designed aerospike nozzle, which could potentially translate to significant fuel weight and volume savings.

Clearly, the requirement to burn the 3-D printed nozzle in a highly fuel-enriched, lowered-temperature environment was a significant compromise, and would not be operationally acceptable. Obviously the melting temperature of Inconel, approximately 1300 °C, is insufficient for operational applications. Swapping the Inconel with a refractory metal would significantly improve the overall survivability of the printed test article.

For example, emerging techniques now allow Tungsten²² printing using Selective Laser Melting laser melting (SLM) technology.^{†††} SLM methods fuse successive layers of pure tungsten powder until a complex component is built. SLM is a major

^{***} Please see the earlier discussion from section IV.H, and the associated results of Figure 16.

^{†††} "Wolfmet 3-D, Excellence in Tungsten," <https://www.wolfmet.com/applications/slm/>.

V. Summary and Conclusion

A need exists for small, inexpensive, and reliable propulsion systems to propel small satellites below the NanoSat size of 10kg. In particular, the rise in popularity of CubeSats is flooding orbits with small spacecraft, many of which rely on reaction wheels for limited maneuvering capabilities. Chemical rockets, used to propel many existing spacecraft, see proportionally large gains from small gains in nozzle performance. This, this paper revisits the Aerospike nozzle -- well-known volumetrically efficient technology for altitude compensation -- for small scale spacecraft propulsion systems where the benefits of modern 3-D printing technology can be brought to bear.

To date, aerospike nozzles have not been seriously considered for small satellite (*SmallSat*) propulsion systems due to the complexity of the plug systems support structures, and the associated manufacturing difficulties that do not scale well to small sizes. Furthermore, due to the relatively small annular throat gap and associated boundary layer hearing, for a given thrust level the aerospike nozzles experience significantly higher heating levels that do conventional nozzles. The ability to manage this excess heating is exacerbated at small scales. Using conventional materials, SmallSat-scale aerospike nozzles would require external cooling or otherwise experience limited operating lifetimes.

Fortunately, the emergence of 3-D metallic printing for refractory metals like tungsten, niobium, molybdenum, and rhenium offers a potential breakthrough that may allow the advantages of the aerospike nozzle to be realized for SmallSat operations. These refractory materials have been traditionally used in applications where their exceptional heat and wear resistance are required. Recently, several companies in Germany, the United States, Japan and other countries have perfected core technologies that overcome the problem of turning refractory metals into 3-D printing materials. The refractory metal spherical powders for 3-D printing are now available in bulk, and are ready to be applied in the key components of aerospace industry.

Aerospike nozzles provide two major advantages of interest over existing state-of-the-art bell nozzles. First, they have superior over-expanded performance that does not lead to normal shockwaves that plague bell nozzles. Second, for in-space vacuum conditions, aerospikes have the potential to be lighter and shorter than bell nozzles of comparable thrust levels and expansion ratios. Previous aerospike testing in literature was performed at a larger scale using conventional fabrication methods. Widespread aerospike hot fire data is limited due to low technological readiness; additionally, thermal degradation of aerospike nozzle throats remains a primary issue of concern that limits their utility. An existing small spacecraft propulsion system prototype previously developed at the Utah State Propulsion Research Lab provided a ready platform to integrate and test the proposed small aerospike nozzles.

In order to assess the feasibility of 3-D printing aerospike nozzles for SmallSat propulsion applications, a series of experiments were conducted to compare the system performances using both fixed-geometry low (2.06:1) and higher (8.5:1) expansion ratio nozzles, against the same system retrofitted to use the higher (8.5:1) expansion ratio aerospike nozzle. The spike contour downstream of the nozzle throat was calculated using the methods of Lee and Thompson to ensure assures that the flow along the nozzle spike will remain nearly isentropic and free of strong shock waves, even for highly over-expanded flow conditions. The geometry upstream of the throat was chosen as Von Karman-type of ogive that minimized the stagnation area and associated heating on the exposed frontal area of the spike support.

The first version of the aerospike nozzle was fabricated using conventional methods, and featured a graphite sleeve to withstand the heating loads. Later the design was reproduced using Direct Metal Laser Sintering (DMLS) at the NASA Marshall Space Flight Center. The entire assembly including threads, center spike, and mounting threads was printed 718-Inconel using an EOS-*M290* DMLS powder bed machine.²³ The printed threads were designed to directly interface the nozzle assembly to the existing thruster motor case.

Multiple Test Burns were collected for the low and high expansion ratio conical nozzles and the aerospike nozzle under both ambient and vacuum test conditions. The ambient tests of both the fixed-geometry and aerospike nozzles were performed in both the Utah State University's (USU) Campus Propulsion Research Laboratory test cell. Whereas, the vacuum tests were performed at the NASA Marshall Space Flight Center's Chemical Synthesis and Testing Laboratory using a small vacuum chamber. The altitude compensating properties of the aerospike nozzle are well demonstrated by these data plots. Results indicate an average increase in specific impulse greater than seconds is possible by switching from a bell nozzle to a similarly designed aerospike nozzle. In fact, during the vacuum testing the aerospike acted like a nozzle of far larger expansion ratio than had physically been constructed.

For the legacy hybrid thruster two motor case lengths are available; a 1-G configuration that accepted a fuel grain of length up to 6.85 cm, and a 2-G configuration that accepted a longer fuel grain with length of up to 12.69 cm. The choice of motor length significantly influenced the operating oxidizer-to-fuel ratio for the system. The shorter motor

resulted in O/F ratios that were near or above the stoichiometric point; whereas, the longer motor resulted in fuel-rich O/F values with significantly lower combustion temperatures.

For this testing campaign, the printed nozzle was fabricated from 718-Inconel as a cost-saving measure. Manufacturing was funded under a cooperative agreement, with the part being built as a "ride-along" using spare build volume during the printing of another component for NASA Space Launch System. When the 3-D printed Inconel aerospike nozzle was first tested in the vacuum chamber using the shorter grain motor, the higher operating temperatures caused the nozzle to fail almost immediately after the motor reached steady state operating conditions. When the longer motor was used, the 3-D printed nozzle survived multiple burns, each reaching steady-state operating conditions with no visible structural degradation or throat erosion. Thus, the feasibility of 3-D printing small-scale aerospike nozzles for a hybrid propellant thruster, achieving a more compact form factor and a net-performance advantage, was successfully demonstrated. As a volumetrically-efficient drop in replace for conventional fixed-geometry nozzles for small spacecraft propulsions systems, the 3-D printed aerospike offers proven performance advantages.

The requirement to burn the 3-D printed Inconel nozzle in a highly fuel-enriched, lowered-temperature environment was a significant compromise, and would not be operationally acceptable. However, fabricating the aerospike nozzle using the refractory metal Tungsten would allow operation at much higher burn temperatures, and would significantly improve the overall survivability of the printed test article. Tungsten has the highest melting temperature (of any metal in pure form). Further, Tungsten does not oxidize at high temperatures and would very likely allow the aero-spike motor to be operated erosion-free near stoichiometric conditions for an extended period without the need for active cooling. Emerging techniques now allow Tungsten printing using Selective Laser Melting laser melting (SLM) technology and represents a potentially fruitful direction of endeavor for follow-in research activities.

Acknowledgements

The authors would like to acknowledge NASA MSFC for their continued funding of this project through Multiple-Use Technologies Co-Operative Research Agreements. These agreements "*Vacuum Test and Plume Contamination Measurements of a Novel Green- Propellant Thruster for Small Spacecraft*," Contract No. NNM16AA01A, March 2016, and "*Performance Optimization of 3-D Printed Hybrid Rocket Fuel Materials*," Contract No. NNM17AA09A, June 2017, in part funded the work presented in this paper. The authors would like to thank MSFC ER-23 for providing access to the required NASA facilities including the vacuum and altitude chambers and the instrumentation used to collect the presented vacuum-test data. We are especially grateful for MSFC employees Kevin Pedersen, Carlos Diaz, and Daniel Cavender for their technical support and expert advice during this project.

References

- ¹ G. P. Sutton and O. Biblarz, *Rocket Propulsion Elements*, 7th ed., New York: Wiley, 2001, Chapt. 4., ISBN 9788126525775. <https://pdfs.semanticscholar.org/6cce/fa84a00b396c5b50b66063772f4851392b8f.pdf>
- ² Henzel, D. K., and Huang, D. H., "Design of Liquid Propellant Rocket Engines," *Progress in Astronautics and Aeronautics*, American Institute of Aeronautics and Astronautics, Washington DC, 1992, Chapter 4. <https://ntrs.nasa.gov/archive/nasa/casi.ntrs.nasa.gov/19710019929.pdf>
- ³ Rao, G., V., R., "Recent Developments in Rocket Nozzle Configurations", *ARS Journal*, Vol. 31, No. 11 (1961), pp. 1488-1494. <https://doi.org/10.2514/8.5837>
- ⁴ Ladeinde, T., Chen, H., "Performance Comparison of a Full-Length and a Truncated Aerospike Nozzle," AIAA 2010-6593, *46th AIAA/ASME/SAE/ASEE Joint Propulsion Conference & Exhibit, Nashville TN, July, 2010*. <https://doi.org/10.2514/6.2010-6593>
- ⁵ Bui, T., Murray, J. R., Bartel, C. A., Cesaroni, A., and Dennet, M., "Flight Research of an Aerospike Nozzle Using High Power Solid Rockets," AIAA 2005-3797, *41st AIAA/ASME/SAE/ASEE Joint Propulsion Conference & Exhibit, Tuscon, AZ, July, 2005*. <https://doi.org/10.2514/6.2005-3797>
- ⁶ Anon., "3-D Printed Composites Materials Markets – 2018," Report No. SMP-3DPCOMP-1218, Published December 12, 2018, <https://www.smartechpublishing.com/reports/3d-printed-composites-materials-markets-2018/>
- ⁷ Lee, C. C., and D. D. Thompson, D. D., "FORTRAN Program for Plug Nozzle Design," NASA TM X-53019, Huntsville, Alabama, 1964. https://archive.org/details/nasa_techdoc_19630012259/page/n1

-
- ⁸ Ferrari, C., "Bodies of Revolution with Minimal Drag Coefficient and Low Heat Transfer at High Supersonic Speeds," *J. Fluid Dynamics*, Vol. 3, No. 5, Sept. 1968, pp. 52-58. <https://link.springer.com/article/10.1007/BF01029537>
- ⁹ Maxey, K., "Metal Sintering Meets Industrial Needs with the EOS M 290," Engineering.com, June 20, 2014, <https://www.engineering.com/DesignerEdge/DesignerEdgeArticles/ArticleID/7829/Metal-Sintering-Meets-Industrial-Needs-with-the-EOS-M-290.aspx>.
- ¹⁰ Whitmore, S. A., Stephen L. Merkley, Tonc, L., and Mathias, S. D., "Survey of Selected Additively Manufactured Propellants for Arc Ignition of Hybrid Rockets", *Journal of Propulsion and Power*, Vol. 32, No. 6 (2016), pp. 1494-1504. <http://dx.doi.org/10.2514/1.B36106>.
- ¹¹ Mathias, S. D., Whitmore, S. A., and Harvey, R., "High Voltage Breakdown and Arc-Tracking Mechanism of Thermoplastics with Applications to Hybrid Rocket Arc-Ignition," AIAA 2017-4601, *53rd AIAA/ASME/SAE/ASEE Joint Propulsion Conference & Exhibit*, Atlanta, Georgia, 9-12 July - 2017. <https://doi.org/10.2514/1.B35595>
- ¹² Whitmore, S. A., "Additively Manufactured Acrylonitrile-Butadiene-Styrene-Nitrous-Oxide Hybrid Rocket Motor with Electrostatic Igniter", *J. Propulsion and Power*, Vol. 31, No. 4 (2015), pp. 1217-1220. <https://doi.org/10.2514/1.B35681>
- ¹³ Whitmore, S. A., Inkley, N. R., Merkley, D. P., and Michael I. Judson, M. I., "Development of a Power-Efficient, Restart-Capable Arc Igniter for Hybrid Rockets", *Journal of Propulsion and Power*, Vol. 31, No. 6 (2015), pp. 1739-1749. <https://doi.org/10.2514/1.B35595>
- ¹⁴ Whitmore, S. A., and Bulcher, A. M., "Vacuum Test of a Novel Green-Propellant Thruster for Small Spacecraft", AIAA 2017-5044, *53rd AIAA/SAE/ASEE Joint Propulsion Conference, AIAA Propulsion and Energy Forum*, Atlanta GA., July 2017, <https://doi.org/10.2514/6.2017-5044>
- ¹⁵ Whitmore, S. A., "Three-Dimensional Printing of "Green" Fuels for Low-Cost Small Spacecraft Propulsion Systems", *Journal of Spacecraft and Rockets*, Vol. 55, No. 1 (2018), pp. 13-26. <https://doi.org/10.2514/1.A33782>
- ¹⁶ Armstrong, Isaac W., MS Thesis, Department of Mechanical and Aerospace Engineering, Utah State University, May 2019. <https://digitalcommons.usu.edu/etd/7428/>
- ¹⁷ Anderson, J. D., *Modern Compressible Flow*, 3rd Edition, New York: The McGraw Hill Companies, Inc., 2003, Chapter 4, pp. 127-187. ISBN-13: 978-0072424430. <https://libcat.lib.usu.edu/search/i0070016542>
- ¹⁸ Whitmore, S. A., Peterson, Z. W., and Eilers, S. D., "Comparing Hydroxyl Terminated Polybutadiene and Acrylonitrile Butadiene Styrene as Hybrid Rocket Fuels," *Journal of Propulsion and Power*, Vol. 29, No. 3, 2013, pp. 582-592. <https://doi.org/10.2514/1.B34382-592>.
- ¹⁹ Gordon, S., and McBride, B. J., "Computer Program for Calculation of Complex Chemical Equilibrium Compositions and Applications," NASA RP-1311, 1994. <https://www.grc.nasa.gov/www/CEAWeb/RP-1311.pdf>
- ²⁰ Whitmore, S. A., and Stephen L. Merkley, S. L., "Effects of Radiation Heating on Additively Printed Hybrid Fuel Grain O/F Shift", AIAA 2016-4867, *52nd AIAA/SAE/ASEE Joint Propulsion Conference, AIAA Propulsion and Energy Forum*, (AIAA 2016-4867) Salt Lake City UT USA, July 2016. *Accepted for Publication J. Propulsion and Power, May 2019*. <http://dx.doi.org/10.2514/6.2016-4867>
- ²¹ Hagemann, G., Nguyen, T. V., and Dumnov, G. E., "Advanced Rocket Nozzles," *Journal of Propulsion and Power*, Vol. 14, No. 5, September -October 1998, pp. 620-634. <https://doi.org/10.2514/2.5354>
- ²² Sidambe, A. T., Tian, Y., Prangnell, P. B., and Fox, P., "Effect of Processing Parameters on the Densification, Microstructure and Crystallographic Texture During the Laser Powder Bed Fusion of Pure Tungsten," *International Journal of Refractory Metals and Hard Materials*, Vol. 8, Jan. 2019, pp. 254-263. <https://doi.org/10.1016/j.ijrmhm.2018.10.004>
- ²³ Maxey, K., "Metal Sintering Meets Industrial Needs with the EOS M 290," Engineering.com, June 20, 2014, <https://www.engineering.com/DesignerEdge/DesignerEdgeArticles/ArticleID/7829/Metal-Sintering-Meets-Industrial-Needs-with-the-EOS-M-290.aspx>.